



HAL
open science

A climatology of infrasound detections in northern Norway at the experimental ARCI array

Láslo Gerardus Evers, Johannes Schweitzer

► **To cite this version:**

Láslo Gerardus Evers, Johannes Schweitzer. A climatology of infrasound detections in northern Norway at the experimental ARCI array. *Journal of Seismology*, Springer Verlag, 2011, 15 (3), pp.473-486. 10.1007/s10950-011-9237-8 . hal-00687350

HAL Id: hal-00687350

<https://hal.archives-ouvertes.fr/hal-00687350>

Submitted on 13 Apr 2012

HAL is a multi-disciplinary open access archive for the deposit and dissemination of scientific research documents, whether they are published or not. The documents may come from teaching and research institutions in France or abroad, or from public or private research centers.

L'archive ouverte pluridisciplinaire **HAL**, est destinée au dépôt et à la diffusion de documents scientifiques de niveau recherche, publiés ou non, émanant des établissements d'enseignement et de recherche français ou étrangers, des laboratoires publics ou privés.

A climatology of infrasound detections in northern Norway at the experimental ARCI array

Láslo Gerardus Evers · Johannes Schweitzer

Received: 20 August 2009 / Accepted: 17 March 2011
© Springer Science+Business Media B.V. 2011

Abstract The study of infrasound is experiencing a renaissance in recent years since it was chosen as a verification technique for the Comprehensive Nuclear-Test-Ban Treaty. Currently, 60 infrasound arrays are being installed to monitor the atmosphere for nuclear tests as part of the International Monitoring System (IMS). The number of non-IMS arrays also increases worldwide. The experimental ARCES infrasound array (ARCI) is an example of such an initiative. The detectability of infrasound differs for each array and is a function of the array location and configuration, the state of the atmosphere, and the presence of natural and anthropogenic sources. In this study, a year of infrasound data is analyzed as recorded by ARCI. Contributions of the atmosphere and

the sources are evaluated in both a low- (0.1–1.0 Hz) and high-frequency (1.0–7.0 Hz) pass-band. The enormous number of detections in the low-frequency band is explained in terms of the stratospheric wind and ocean wave activity and compared with the detection of microseism. Understanding the detectability in the low-frequency band is of utmost importance for successfully applying infrasound as a verification technique since small-sized nuclear test will show up in this frequency range.

Keywords Infrasound · Array · Signal detection · Source identification · Acoustic propagation

1 Introduction

Infrasound was first discovered after the violent eruption of the Krakatoa, Indonesia, in 1883. Low-frequency pressure waves were observed at traditional barographs. These appeared to have traveled with the sound speed and up to four passages where noticed at some instruments (Symons 1888). The first microbarometer recordings date from 1908 when a comet, or asteroid, exploded over Siberia in Russia, the so-called Tunguska event (Whipple 1930). The societal and scientific interest in infrasound increased during World War I, e.g., Whipple (1939), and later on in the nuclear testing era (Posey and Pierce 1971). With the

L. G. Evers
Seismology Division, Royal Netherlands
Meteorological Institute, PO Box 201,
3730 AE De Bilt, The Netherlands

L. G. Evers (✉)
Acoustic Remote Sensing Group,
Faculty of Aerospace Engineering, TU Delft,
PO Box 5, 2600 AA Delft, The Netherlands
e-mail: evers@knmi.nl

J. Schweitzer
NORSAR, PO Box 53,
2027 Kjeller, Norway
e-mail: johannes@norsar.no

44 signature of the Limited Test Ban Treaty in 1963,
 45 most interest in infrasound promptly came to a
 46 stop, since nuclear tests were confined to the sub-
 47 surface. Only a few studies could be maintained
 48 (Balachandran et al. 1977; Liszka 1978). In recent
 49 years, the study of infrasound gained renewed
 50 interest because of the Comprehensive Nuclear-
 51 Test-Ban Treaty (CTBT) that opened for signing
 52 in 1996, where it is used as a verification technique
 53 for atmospheric tests (Dahlman et al. 2009).

54 Sources of infrasound are in general large, since
 55 an enormous amount of air has to be displaced
 56 to generate such low frequencies (Gossard and
 57 Hooke 1975). Natural sources are avalanches,
 58 lightning, meteors, oceanic waves, earthquakes,
 59 severe weather, volcanoes, and sprites. Among
 60 anthropogenic sources are explosions, supersonic
 61 flights, military activity, rocket launches, and nu-
 62 clear tests. Identifying the sources of infrasound
 63 out of this zoo of coherent waves in the at-

64 mosphere is one of the major challenges in infra-
 65 sound research.

66 The propagation of infrasound through the
 67 highly dynamic atmosphere plays an important
 68 role in source identification. Infrasound travels
 69 up to thermospheric altitudes of 120 km and ex-
 70periences refractions due to an increase in wind
 71 and/or temperature as a function of altitude.
 72 If the gradients in the propagation velocity are
 73 strong enough, infrasound will be sent back to the
 74 Earth's surface (Drob et al. 2003). There are three
 75 regions in the atmosphere where such gradients
 76 might exist. These are of importance in long-range
 77 sound propagation, i.e., over distances larger than
 78 150 km. The regions are marked by (1) a strong jet
 79 stream at 10 km altitude, near the tropopause;
 80 the combined effect of wind and temperature at
 81 the stratopause, around 50 km altitude; and (3) the
 82 temperature increase in the thermosphere from
 83 100 km and upward.

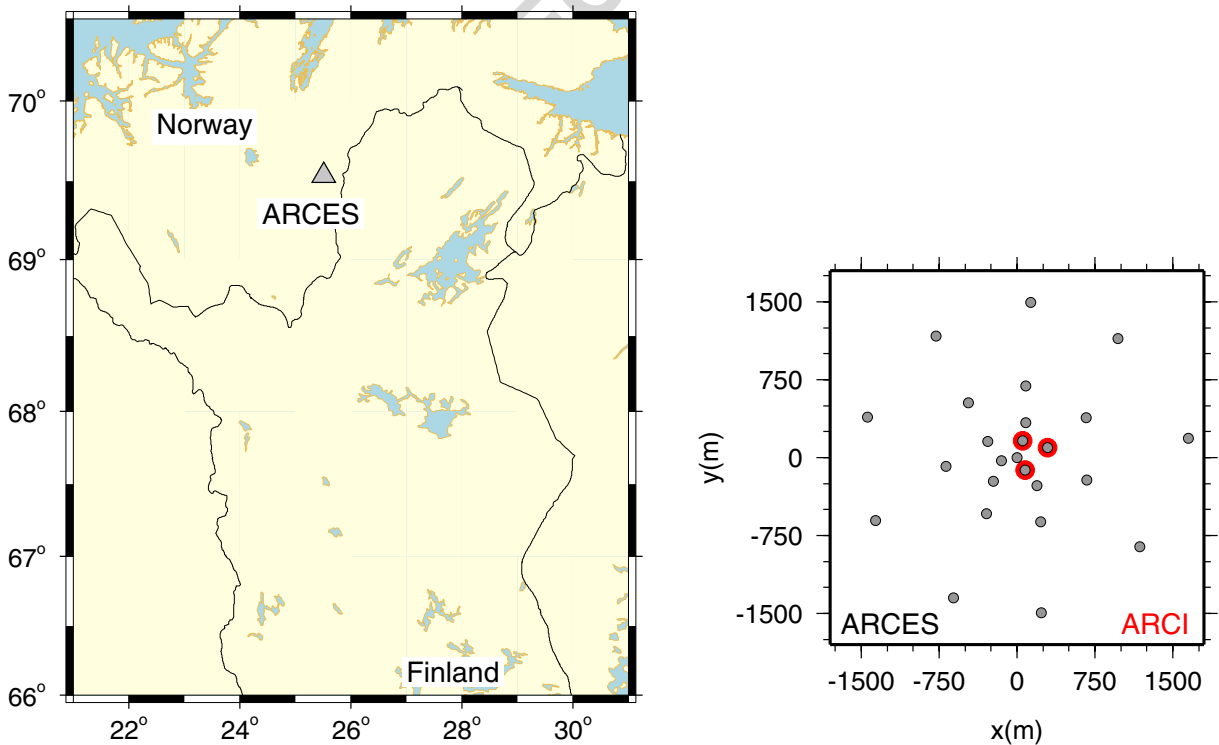


Fig. 1 The location of the ARCES seismic array and positions of the seismometers (*gray dots*). The temporary array ARCI is configured with three microbarometers (*red*

circles), which are co-located with seismometers in the center of the seismic array

84 The aim of this study is to identify the sources
85 around the ARCES array and to build up a clima-
86 tology of station-specific detections. Each infra-
87 sound array has its own detection capabilities as
88 its configuration, the atmospheric conditions, and
89 source characteristics are highly variable as func-
90 tion of geographical location and time. Special
91 attention will be paid to the low-frequency band of
92 0.1 to 1.0 Hz which is of utmost importance for the
93 verification of the CTBT as small-sized nuclear
94 tests (around 1 kT TNT) are expected to generate
95 infrasound of 0.1 to 0.2 Hz (Evers and Haak 2001).
96 It is also this band in which the almost continuous
97 background noise of microbaroms is present that
98 peak around 0.2 Hz (Posmentier 1967).

99 2 The ARCES infrasound array

100 A three-element experimental infrasound array
101 was established at ARCES in March 2008, which
102 will be abbreviated as ARCI (Roth et al. 2008).
103 The purpose of the installation is to gain ex-
104 perience with the simultaneous recording of in-
105 frasonic and seismological data. Figure 1 shows
106 the location and configuration of ARCI. The in-
107 struments are microbarometers of type Martec
108 MB2005 which have a flat frequency response to
109 pressure in the range of 0.01 to 27 Hz. Infrasound
110 measurements are affected by noise due to wind.
111 Therefore, a spatial filter is applied at each in-
112 strument which essentially integrates the pressure
113 field. Doing so, pressure fluctuations with a small
114 coherency length, like those of tens of centimeters
115 associated with wind noise, are partly canceled
116 out. The infrasonic waves of interest remain undis-
117 turbed because of their much larger coherency
118 length of tens to hundreds of meters. Such analog
119 filters can consist of a pipe array with discrete
120 inlets or porous hoses (Hedlin et al 2003). The lat-
121 ter approach is applied at ARCI with four soaker
122 hoses, each with a length of 12 m, connected to the
123 MB2005. For one of the three sites, the hoses are
124 additionally centered in a drainage pipe. Environ-
125 mental restrictions at the ARCES array prevent
126 the installation of larger pipe arrays that require
127 fencing. The applied noise reduction should be
128 considered as minimal. The atmospheric pressure

changes around ARCI are sampled at a rate of 129
80 Hz. 130

3 Data processing and signal detection 131

3.1 The approach 132

The detections of coherent infrasonic signals trav- 133
eling over the array can be achieved by evaluating 134
the Fisher (F) ratio. The F detector has been 135
described in both the time (Melton and Bailey 136
1957) and frequency domain (Smart and Flinn 137
1971). In essence, a statistical hypothesis is tested. 138
Applying a F -detector is attractive because of its 139
well-known statistical distribution. The hypothesis 140
to be tested is that all recordings made by the mi- 141
crobarometers consist of uncorrelated noise. The 142
alternative hypothesis is valid for the case that not 143
only noise is present but also signal. Evaluated 144
are the variance of the noise and the variance 145
of all recordings, which cannot be attributed to 146
the noise since it is common to all recordings. 147
The F detector has been successfully applied in 148
infrasound processing to detected, for example, 149
meteors and microbaroms (Evers and Haak 2001). 150
The processing sequence applied in this study is as 151
follows: 152

- Remove the mean of the recordings. 153
- Band-pass filter with a second-order Butter- 154
worth filter with corner frequencies of 0.1 155
and 1.0 Hz (the low-frequency or microbarom 156
band) and 1.0 and 7.0 (the high-frequency 157
band). 158
- Decimate the data with a factor of 4, to re- 159
duce the data volume in order to minimize 160
the computational efforts, from a 80- to 20-Hz 161
sampling rate. 162
- Define a slowness grid between -0.005 and 163
 0.005 s/m of 100×100 points, forming 10,000 164
beams. 165
- Split the data in segments of 256 samples, 166
which equals a bin of 12.8 s. 167
- Evaluate the Fisher ratio for each beam in 168
each bin (with 50% overlapping bins). 169
- Extract the slowness value, i.e., the backaz- 170
imuth and apparent sound speed, at the maxi- 171
mum Fisher ratio, for each bin. 172

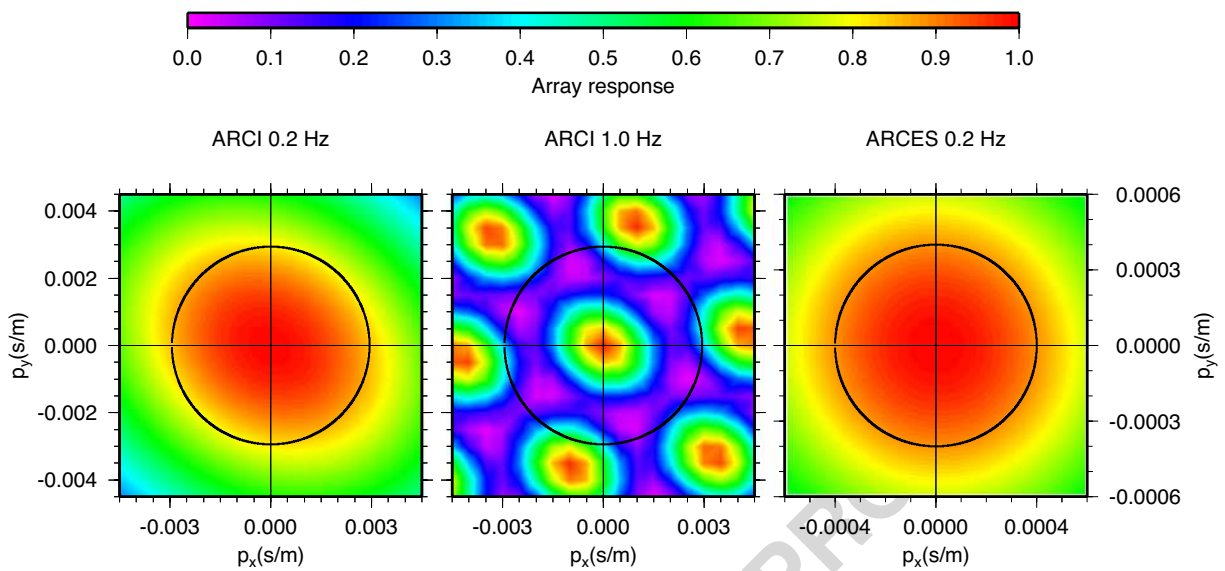


Fig. 2 The array response of ARCI to a 0.2- and 1.0-Hz planar wave (left two frames). The black circle represent an apparent velocity of 340 m/s. The array response of

ARCES is given in the right frame at 0.2 Hz; the black circle corresponds to an apparent velocity of 2,500 m/s

173 The above approach extracts the most coherent
 174 arrival from a data segment. If multiple sources
 175 are active at the same time, preference is given to
 176 the one with the highest F ratio.

177 The array response of ARCI is given in Fig. 2
 178 for a low (0.2 Hz) and higher frequent (1.0 Hz)
 179 planar wave. The limited aperture of ARCI results
 180 in a broad main lobe at 0.2 Hz, but its maximum
 181 can still be confidently determined. At higher
 182 frequencies, spatial aliasing starts to play a role
 183 because of the low number of array elements.
 184 However, at 1.0 Hz, no side lobes are present in
 185 the velocity range of interest.

186 3.2 Detections in the high-frequency band

187 Most sources in the high-frequency band are man-
 188 made. Figure 3 shows the time of occurrence of
 189 events in this band, for the period of March 13,
 190 2008 up to May 14, 2009. There appear to be less
 191 events during the weekends (days 6 and 7), com-
 192 pared to weekdays, and during nighttime. In other
 193 words, most events occur during the working week
 194 and at daytime hours, which clearly indicates that
 195 the sources are of anthropogenic origin. The re-

solved backazimuths with respect to ARCI are
 given in the left frame of Fig. 4. Most events occur
 from an eastern to southwestern direction. Some
 of these can be explained by quarries, mines, and
 military activity, as indicated by the red lines.
 The source of the peak around 190° has not yet
 been identified. Less events find their origin in the
 north, although two distinct peaks, around 290°
 and 330° , indicate activity to the northwest.

3.3 Detections in the low-frequency band

Figure 5 shows the results of the previously de-
 scribed processing approach for ARCI data in
 the low-frequency band between 0.1 and 1.0 Hz.
 The lower frame shows the maximum Fisher ratio
 for each bin. This value is related to the squared
 signal-to-noise ratio (SNR) on the traces (see axis
 on the right). The middle and top frames show
 the resolved apparent sound speed and backaz-
 imuth. Color coded are the number of detections
 within an hour, where five or more detections
 are denoted by red. Here, only detections with a
 SNR larger than 1.0 are plotted, which equals a
 Fisher ratio of four and higher. Such a detection

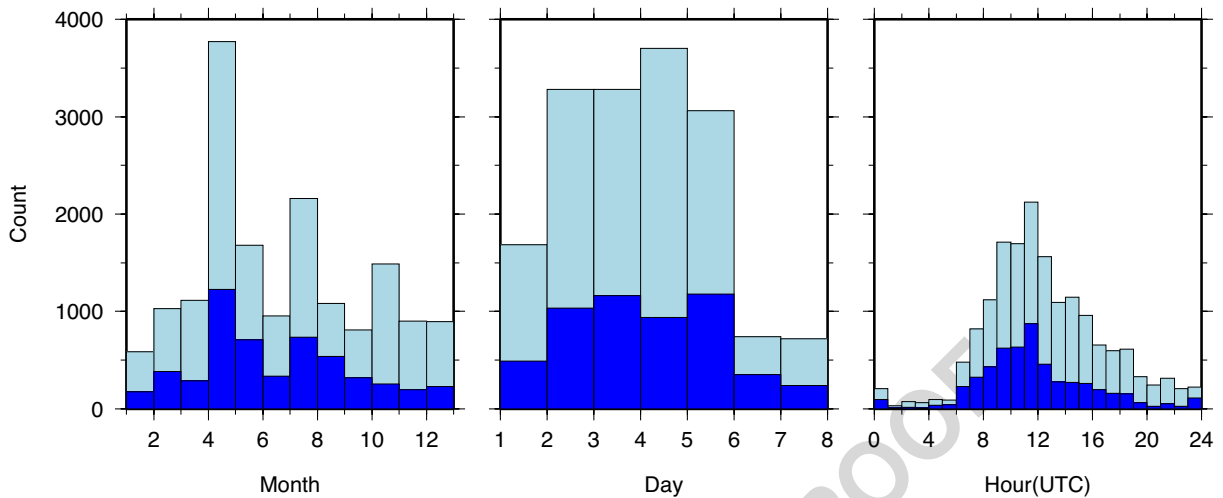


Fig. 3 Results from the array processing of ARCI data in the high-frequency band of 1.0 to 7.0 Hz. The histograms shows the time of occurrence of infrasound events, between March 13, 2008 and May 14, 2009. *Light blue colors* indicate events with a signal-to-noise ratio (SNR) larger

than 1 (or Fisher ratio of 4 and higher). *Dark blue* means a SNR larger than 1.5. The weekday diagram starts with day 1 which is Monday. For the hour histogram, local time in Norway is UTC+2h for summer and UTC+1h for winter

219 will be labeled as an event and is mostly related
 220 to microbarom activity. It follows from the lower
 221 frame of Fig. 5 that signal coherency strongly
 222 fluctuates as function of time. Large changes are
 223 seen from day to day, but there also seems to be a
 224 difference between winter and summertime (May

to September). These are also reflected in the
 225 resolved apparent sound speed and backazimuth. 226
 227 The short time variations in signal coherency show
 228 up as gaps, which means that no events have been
 229 detected. During summer, less coherent events are
 230 detected than in winter, and they appear from 230

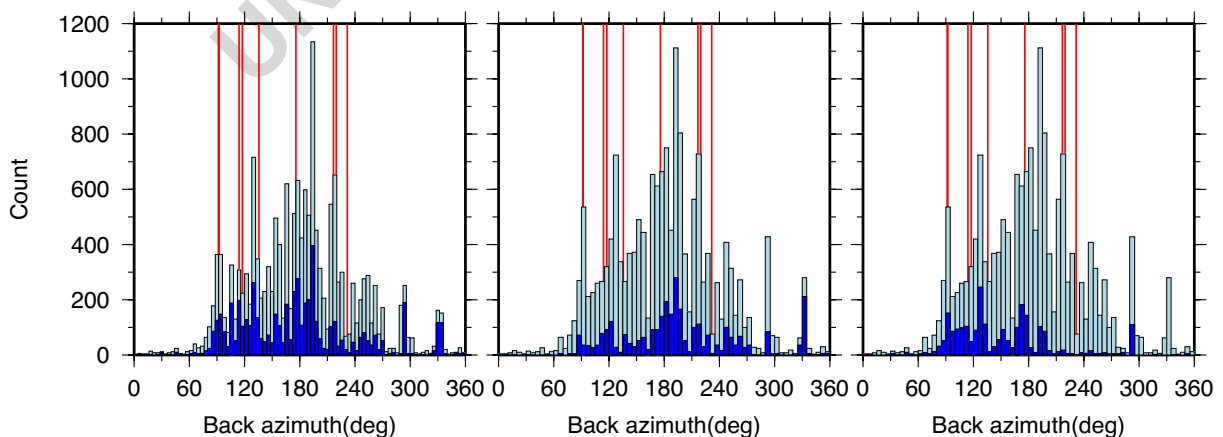


Fig. 4 The number of events (count) as function of the backazimuth for the high-frequency band. Events with a SNR larger than 1 are denoted by *light blue*; *blue* is used for a SNR larger than 1.5. The *red lines* give the backazimuths

toward quarries, mines, and regions of military activity. The *left frame* gives all events; the *middle and right frame* are for winter and summer, respectively

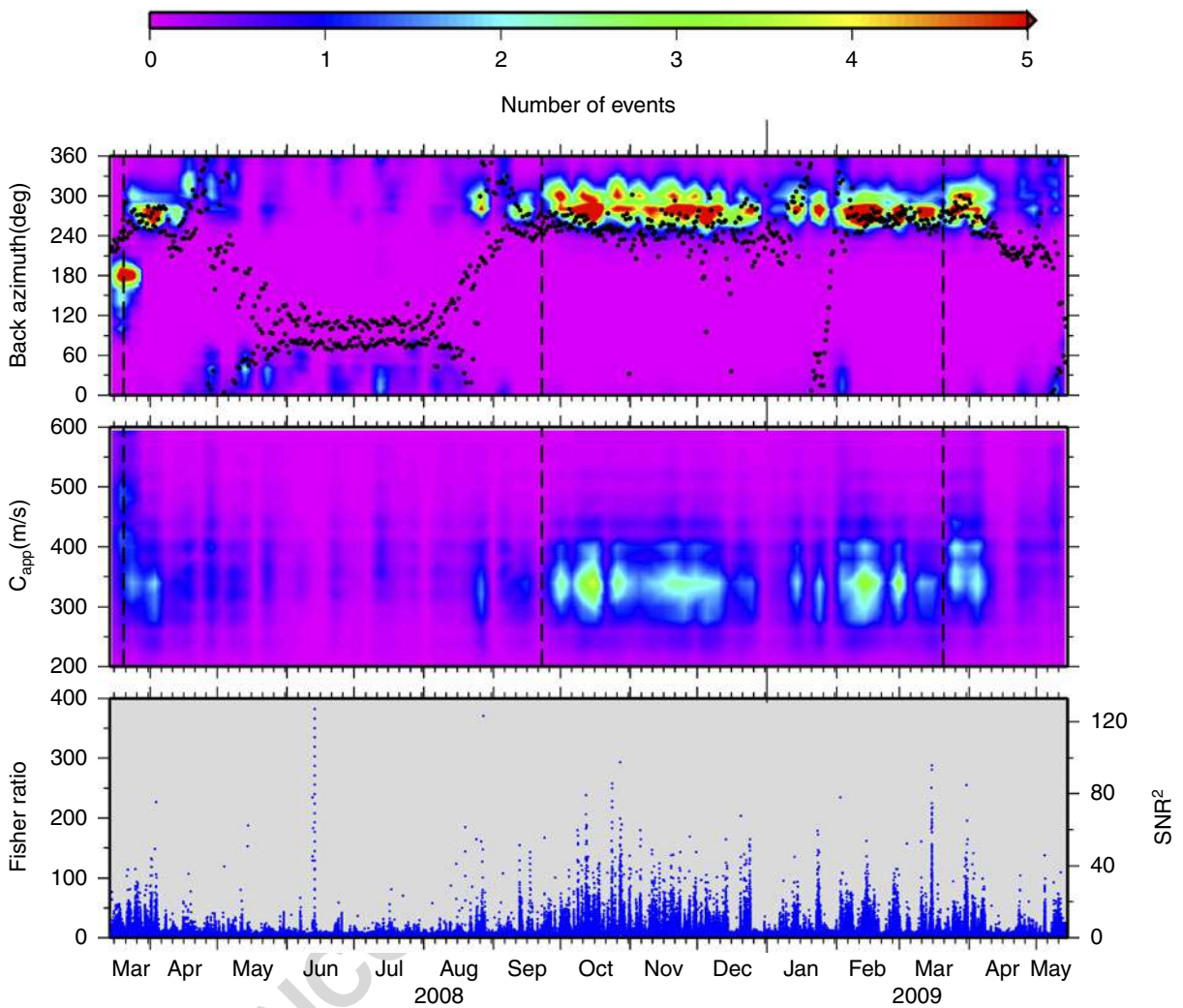


Fig. 5 Results from the array processing of ARCI data in the low-frequency band from 0.1 to 1.0 Hz. The *lower frame* shows the Fisher ratios as function of time, that is, between March 13, 2008 and May 14, 2009. The Fisher ratio is related to the signal-to-noise (SNR) power ratio on the traces (see the axis on the *right*). The *top frames*

gives the resolved apparent sound speed and backazimuth. Color coded are the number events per hour with a SNR larger than 1. Five or more events are indicated by *red colors*. The *black dots* represent the wind direction at 50 km altitude from the ECMWF analysis at 69.50 N, 25.50 E. The equinoxes are indicated by the *vertical dashed lines*

Q1

231 northeastern directions. In winter, events are detected almost continuously and find their origin to the west of ARCI.

232
233
234 Variations in the detectability of infrasound can have several causes. These could be related to the state of the atmosphere and variations of the source (Le Pichon et al. 2009; Evers and Haak 2005). For the atmosphere, contributions along the source–receiver path will be evaluated in the following as well as near receiver effects. The

241 location, time, and strength of the source vary as function of time and will also be analyzed.

4 Contributions of the atmosphere

4.1 General propagation characteristics

245 Atmospheric causes of the variations in the detectability of infrasound are related to two

247 distinct areas in the atmosphere, the stratosphere
 248 and the boundary layer. The boundary layer is
 249 approximately the first kilometer of atmosphere,
 250 within the lower troposphere. The stratosphere
 251 reaches from the tropopause, around 10 km, up
 252 to the stratopause near 50 km altitude. The ther-
 253 mosphere, from 100 km and upwards, is not con-
 254 sidered here because, in the considered frequency
 255 range, thermospheric arrivals are strongly atten-
 256 uated by the highly rarefied upper atmosphere.
 257 These are, therefore, not expected to be observed
 258 over ranges of over 1,000 km (Sutherland and
 259 Bass 2004).

260 4.2 Stratospheric variability

261 The wind in the stratosphere, called the polar
 262 vortex, varies on a seasonal scale. During win-
 263 ter, winds are directed to the east, around the
 264 stratopause on the Northern Hemisphere. These
 265 winds can reach values of over 150 m/s. In sum-
 266 mer, these winds are directed to the west and
 267 somewhat less strong, reaching values of 70 m/s.
 268 Figure 6 shows the wind and temperature near
 269 ARCI, at 69.50 N, 25.50 E, as function of time.
 270 These atmospheric specifications were obtained
 271 from the European Centre for Medium-Range
 272 Weather Forecasts (ECMWF). The wind is split
 273 in a meridional and zonal component. The merid-
 274 ional wind is the south–north component of the
 275 wind and has a positive sign when directed to the
 276 north. A positive sign for the zonal wind, which is
 277 the west–east component, means it is directed to
 278 the east. The change in the zonal wind direction
 279 around the equinox should be noted, which causes
 280 the anisotropy of the medium.

281 The temperature increase, due to presence of
 282 ozone, and strong winds around 50 km altitude
 283 may lead to bending of infrasonic waves back to
 284 the Earth's surface, due to the increase in effective
 285 propagation velocity. Changes in this so-called
 286 stratospheric duct are visible in the surface based
 287 microbarometer recordings of ARCI.

288 4.2.1 Consequences for the high-frequency band

289 For the high-frequency band, a distinction is made
 290 between summer and winter in Fig. 4. It follows

from this figure that events from the west are 291
 more easily detected in winter as the stratospheric 292
 winds are favorable for such propagation. Events 293
 from the east are better detected in summer, but 294
 some show up in wintertime. The detections of 295
 sources which are not affected by the direction of 296
 the polar vortex probably find their origin close to 297
 the array, i.e., at distances less than 150 km, where 298
 tropospheric propagation is still dominant. 299

4.2.2 Consequences for the low-frequency band 300

In Fig. 5, the wind direction at 50 km altitude 301
 is superimposed on the resolved backazimuths, 302
 for the low frequency band. Clearly, the detec- 303
 tion of coherent infrasound is guided by the 304
 stratospheric wind. In winter, microbarom energy 305
 from the Northern Atlantic Ocean is recorded. As 306
 the winds turn around the equinox, microbarom 307
 energy from the east is being detected. 308

As can be seen in Fig. 6, an abrupt change in 309
 the winds and temperature occurred in the winter 310
 of 2009, between late January and early Febru- 311
 ary. Such changes are related to a major sudden 312
 stratospheric warming (SSW; Holton 1979). The 313
 temperature increases by 50°C in the stratosphere, 314
 in only a couple of days, and the polar vortex 315
 changes its direction. The major SSW also had 316
 its effect on the infrasound detections (see also 317
 Fig. 5). Suddenly, microbaroms from the east are 318
 detected because of the change in direction of the 319
 polar vortex, which is unusual in winter (Evers 320
 and Siegmund 2009). 321

4.3 Variability in the boundary layer 322

The state of the boundary layer above the array 323
 can cause de-correlation of the signals. A tur- 324
 bulent atmosphere affects the signal coherency 325
 which leads to a decrease of the detection capa- 326
 bility. The summer boundary layer is far more 327
 turbulent than the winter one. Heating of the 328
 boundary layer due to solar radiation generates a 329
 high degree of mixing. This effect is also visible 330
 on a daily scale where the nighttime boundary 331
 layer stabilizes as the influence of solar radiation 332
 decreases. 333

Figure 7 shows the signal coherency, by means 334
 of the Fisher ratio, for July and October 2008 335

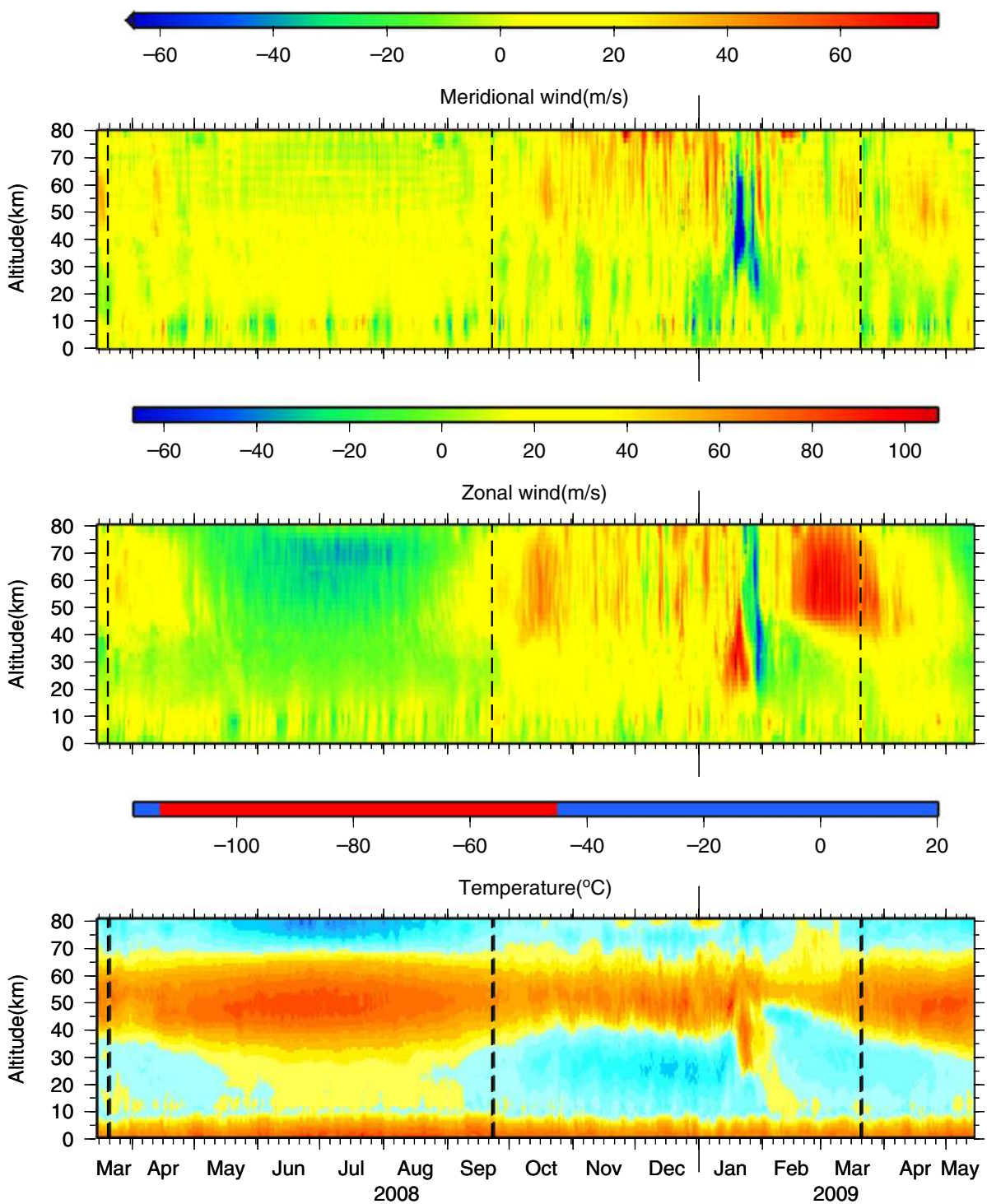


Fig. 6 The temperature and wind from the analyzes provided by the ECMWF. These models are available on a $0.5 \times 0.5^\circ$ grid, each 6 h/day. The grid node closest to ARCI is chosen, being 69.50° N, 25.50° E. The wind and temperature is modeled at 91 levels up to an altitude of

approximately 80 km. All values for the meridional wind lower than -65 m/s are colored *blue*, for plotting purposes, the actual lowest value is -140 m/s. The equinoxes are indicated by the *vertical dashed lines*

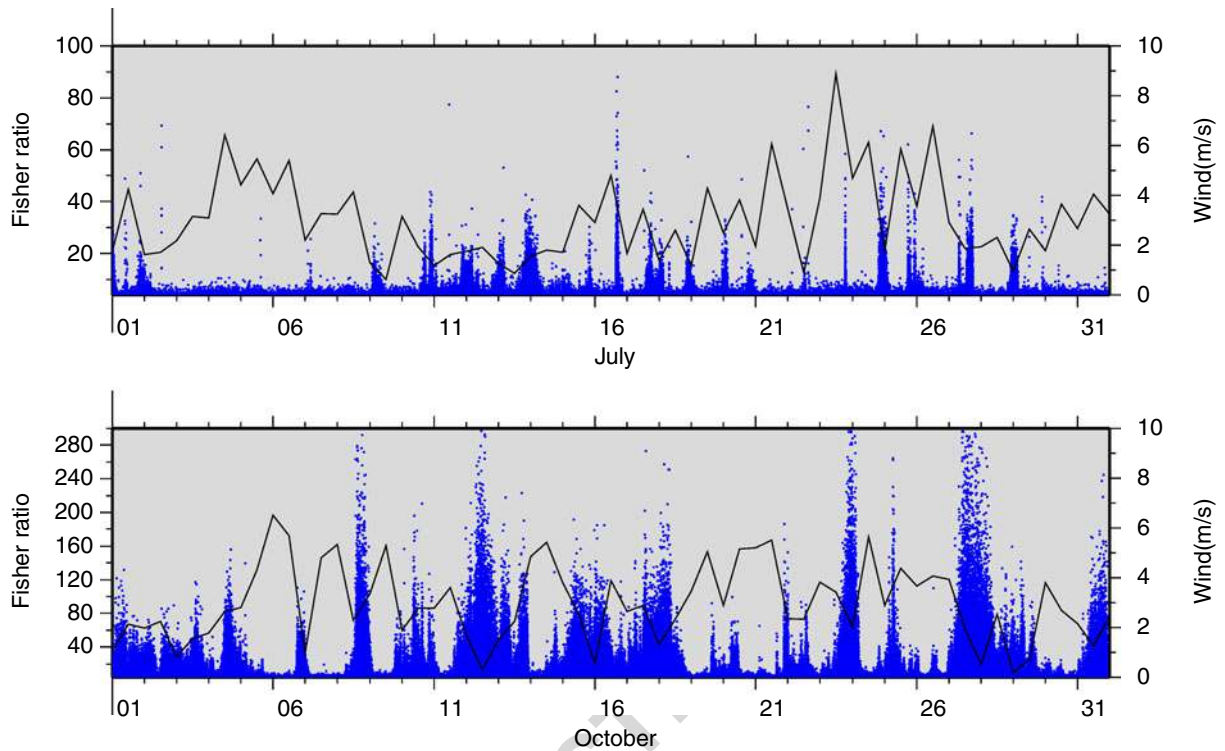


Fig. 7 The Fisher ratios for July (*top*) and October 2008 (*bottom frame*), for the low-frequency band. Superimposed are the wind strengths, as *solid black lines*, at the first

level of the ECMWF models at 69.50 N, 25.5 E. This first level corresponds to an altitude slightly above the Earth's surface

Q1

336 in the low-frequency band. Superimposed are the
 337 wind strengths from ECMWF models, at 69.50
 338 N, 25.50 E, for the first level which is slightly,
 339 i.e., around 300 m, above the Earth's surface. It
 340 follows from this figure that the wind strength in
 341 summer varies on a daily basis. It peaks during
 342 daytime and decreases at night when the influence
 343 of solar radiation is reduced. The reduction in
 344 wind leads to an increase in the detectability of in-
 345 frasound which is reflected by higher Fisher ratios.
 346 Wind variations in winter have longer periods, but
 347 also here an increase in wind leads to a decrease in
 348 performance of the array.

349 5 Specifications of the microbarom sources

350 5.1 Description of microbarom source

351 The source generating the signals, in the low-
 352 frequency band, varies in strength over time. The

microbaroms are generated by the non-linear in- 353
 354 teraction of oceanic waves, which often occurs 354
 355 in the vicinity of low-pressure systems over the 355
 356 oceans. The interference of almost oppositely 356
 357 traveling waves leads to pressure signals in both 357
 358 the atmosphere and the solid Earth, i.e., micro- 358
 359 seism. The signals have a dominant frequency 359
 360 around 0.2 Hz, which is double the frequency 360
 361 of the oceanic waves. The amplitude of induced 361
 362 pressure waves (I_S) is, in first order, propor- 362
 363 tional to the squared multiplication of the wave 363
 364 height (a) and frequency (ω), thus $I_S \sim (a\omega)^2$ 364
 365 (Posmentier 1967). To accurately predict the gen- 365
 366 eration of microbaroms, the directional spectra of 366
 367 oceanic waves should be evaluated to identify the 367
 368 almost oppositely traveling waves and their peri- 368
 369 ods (Kedar et al. 2008). Here, it is assumed that 369
 370 the waves are interacting near the maximum of 370
 371 the squared multiplication of the wave height and 371
 372 frequency. This allows for an efficient calculation, 372
 373 to get an indication of the source activity (Evers 373

374 and Haak 2001). An independent approach will
 375 also be tested where the occurrence of micro-
 376 seism in the seismic recordings of ARCES are
 377 evaluated.

378 5.2 Wave height and frequency from oceanic
 379 wave models

380 Figure 8 shows the backazimuths in the direction
 381 of microbarom activity in the Atlantic and Pacific

Ocean, from 12-hourly oceanic wave models provided by the ECMWF. The source intensity, I_s , is also estimated. The observed backazimuths of the infrasound and direction of microbarom activity coincide throughout the seasons. The detection of microbaroms is also clearly related to the direction of the stratospheric winds (Garcés et al. 2004; Le Pichon et al. 2006). During the SSW which occurred in the winter of 2009, there is a sudden change in resolved backazimuths. Microbarom energy from the Pacific Ocean is detected, during

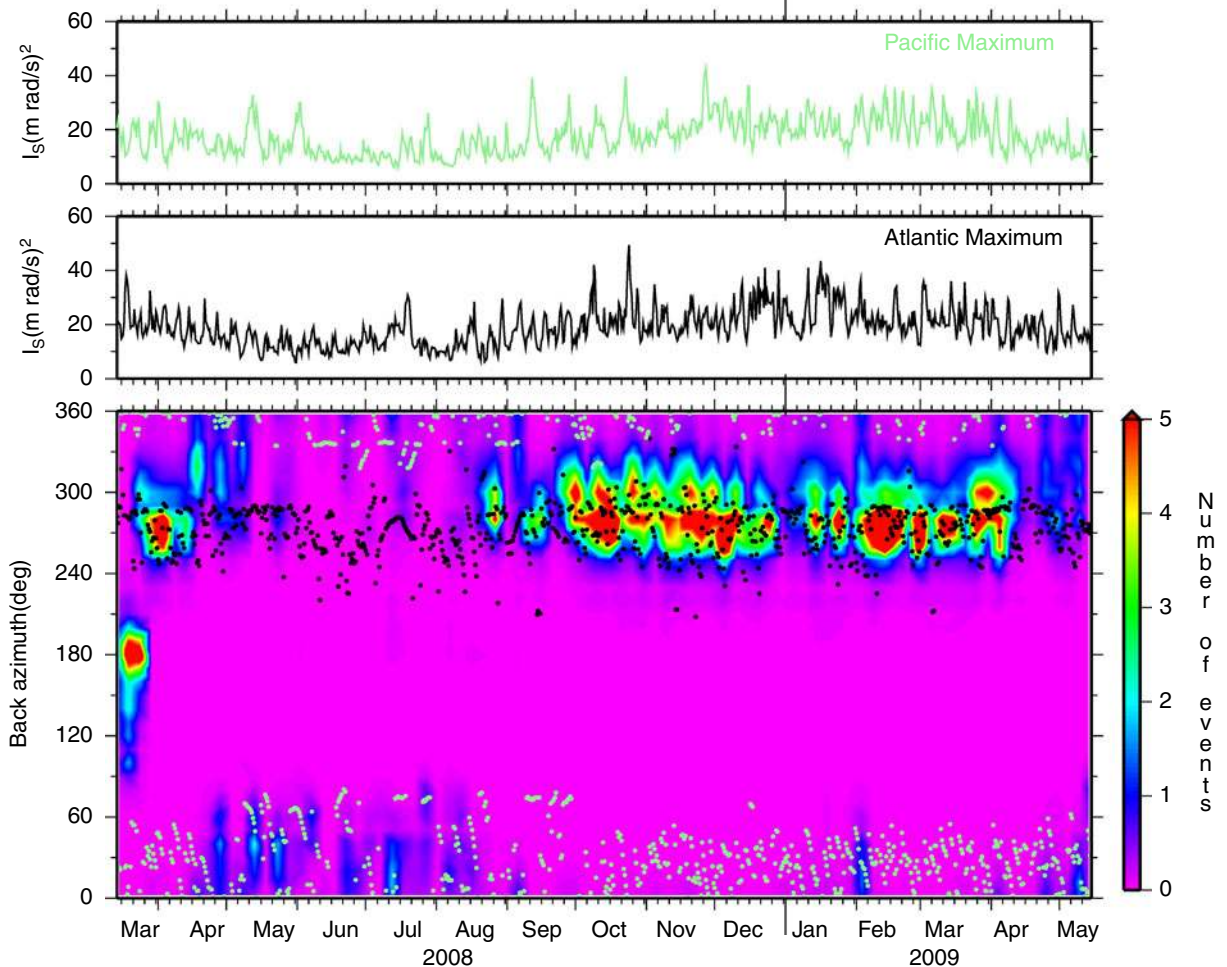


Fig. 8 An estimate of the microbarom activity in the Atlantic (black dots) and Pacific Ocean (green dots). The dots give the directions, i.e., backazimuths, to the Atlantic and Pacific maxima. The retrieved directions, in the lower

frame, and source intensities (I_s , in the upper frames) are calculated from 12-hourly oceanic wave models from ECMWF provided at each $0.5 \times 0.5^\circ$

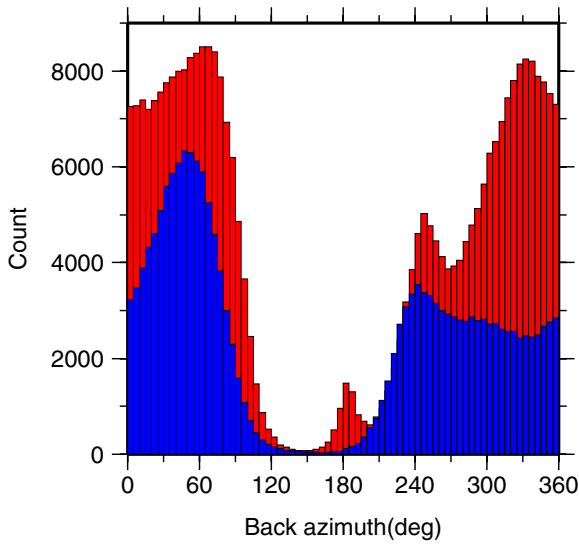


Fig. 9 Detections of microseism at the ARCES array. These detections are split in summer (in red, April through September) and winter (blue)

393 a short period in early February. This indicates
 394 that the low-frequency energy detected during
 395 summer might also find its origin on the Pacific
 396 Ocean.

5.3 Comparison with microseismic detections 397

Seismic data from the ARCES array (see Fig. 1) 398
 are processed to detect energy from microseism. 399
 The processing sequence is as follows: 400

- Band-pass filter with a third-order Butterworth filter with corner frequencies of 0.1 and 0.4 Hz. 401-402-403
- Decimate the data with a factor of 8, from a 40- to 5-Hz sampling rate. 404-405
- Split the data in a window of 20 s. 406
- Apply a frequency–wavenumber analysis, between 0.15 and 0.25 Hz, by moving this window with 6 s. 407-408-409
- Calculate a beam and measure the maximum amplitude in the window. 410-411

The array response of ARCES for a 0.2-Hz 412
 planar wave is given in Fig. 2. At such low frequen- 413
 cies, the main lobe is quite broad but its maximum 414
 can still be determined with enough accuracy for 415
 this study, since only a rough estimate ($\pm 5^\circ$) of 416
 the backazimuth is sufficient. The detections of 417
 microseism at ARCES are shown in Fig. 9. A 418
 total of 6.4 million coherent seismic arrivals are 419
 detected between 0.15 and 0.25 Hz. This number is 420

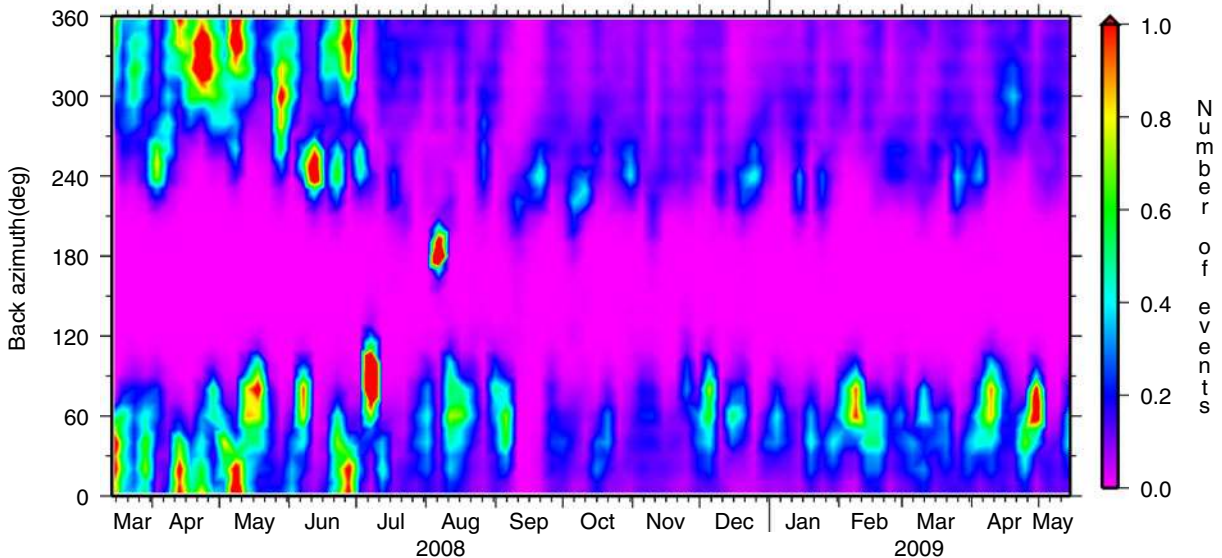


Fig. 10 The occurrence of microseism at the ARCES array. Detections are contoured as function of time and backazimuth. The detections are averaged per hour and one or more detections are indicated by red colors

421 significantly reduced by only considering apparent
422 velocities between 2.0 and 3.0 km/s, which re-
423 sembles the Rayleigh wave propagation velocity.
424 A further reduction is achieved by only allowing
425 for detections with a large signal coherency. The
426 signal coherency is determined by the normalized
427 frequency–wavenumber spectrum. If a threshold
428 of 0.8 is chosen for the spectral density, the num-
429 ber of detections is reduced to 494,290. No en-
430 ergy appears at ARCES from roughly a south to
431 southeastern direction, as expected from its geo-
432 graphical location. Microseism are present from
433 the east to the west, via the north, indicating local
434 and distant ocean wave activity, i.e., the North
435 Atlantic and north of the Siberian coastline when
436 the Arctic is not covered by sea ice or eventually
437 from the northern Pacific Ocean. A peak pops
438 up around 180° during summer (April through
439 September).

440 The microseismic detections are represented as
441 function of time in Fig. 10, in a similar way as
442 the microbaroms (see Fig. 5). Microseismic energy
443 is almost continuously being detected probably
444 from nearby sources and the Atlantic, the Arc-
445 tic, and possibly the Pacific Oceans. Microbarom
446 detections, on the other hand, showed a strong
447 directionality throughout the seasons.

448 6 Discussion and conclusion

449 Infrasound data from ARCI have been processed
450 by evaluating the Fisher ratio over the period
451 of March 13, 2008 up to May 14, 2009. With a
452 detection threshold at a SNR of 1, 1.8 million
453 events are detected between 0.1 and 1.0 Hz and
454 16,475 events between 1.0 and 7.0 Hz. Detections
455 in the low-frequency band are mostly related to
456 the interaction of oceanic waves which leads to
457 microbaroms. In the high-frequency band, mainly
458 man-made events are detected which are related
459 to mining and military activity. Similar findings
460 have been reported by Le Pichon et al. (2008).

461 The characteristics of the medium, i.e., wind
462 and temperature structure up to stratospheric al-
463 titudes, and the source have been derived from
464 ECMWF models. A clear relation has been shown
465 between upper atmospheric winds and the direc-
466 tionality of the detections for the low-frequency

band. These seasonal changes are also partly vis- 467
ible in the high-frequency band. In winter, the 468
sources to the west are detected while preference 469
is given to sources in the east during summer. 470
The state of the boundary layer, or turbulence 471
and low-level winds, partly determines the signal 472
coherency. In summer, there is a daily variation 473
caused by the influence of solar radiation. A more 474
stable boundary layer during nighttime leads to 475
less coherency loss. 476

477 In addition, microbarom activity has been esti-
mated by evaluating the ocean wave height and 478
period. ARCI is sensitive to microbaroms from 479
the Atlantic Ocean in winter. Microbarom energy 480
from the east is detected during summer. This 481
anisotropic behavior was also identified during a 482
period of only a couple of days, related to a SSW. 483
A sudden change was noted from the detection 484
of microbarom energy from the Atlantic Ocean to 485
those from the Pacific Ocean. 486

487 The importance of taking into account both
the characteristics of the medium and the source 488
is illustrated by comparing Figs. 5 and 8. The 489
detections move from west (270°) to northwest 490
(330°) during March and April 2008. It follows 491
from Fig. 8 that the sources, microbaroms in the 492
Atlantic Ocean, are occurring with a more or less 493
stable backazimuth between 270° and 300°. The 494
stratospheric wind, on other hand, is varying from 495
southwest to north during this period. Therefore, 496
this change in the resolved backazimuths should 497
be attributed to the wind which enables the detec- 498
tion of an unknown source to the south of ARCI. 499

500 Another change is visible, in Fig. 8, between
October 2008 and April 2009. The resolved back- 501
azimuths tend to move somewhat from the north- 502
west to the west. The cause should be related to 503
the source, as the wind shows no evidence for 504
such translation. Whether this change relates to 505
the southward movement of sea ice during winter 506
remains to be investigated. It is hypothesized that 507
the sea ice blocks the northward propagation of 508
oceanic waves. Consequently, the generation of 509
microbaroms is limited up to a certain longitude. 510
This is also indicated by the microseism detec- 511
tions. The source seems limited in its northward 512
propagation during winter (see Fig. 10). 513

514 The seasonal variations in microbarom detec-
tions also follow from the comparison with the 515

516 microseismic detections. The highly dynamic and
 517 anisotropic nature of the atmosphere can prohibit
 518 the detection of energy from certain directions.
 519 The ocean wave activity, i.e., generation of mi-
 520 croseism, is almost continuously present from the
 521 Atlantic and Pacific Ocean. The microbaroms ap-
 522 pear from 270° during winter, while the micro-
 523 seism have a dominant backazimuth of 240°. The
 524 latter direction coincides with the location found
 525 by Essen et al. (2003) which was just off coast
 526 of Norway. The microbaroms are probably gen-
 527 erated in the deep ocean as the direction points to
 528 a location similar to the one found by Evers and
 529 Haak (2001) and Kedar et al. (2008), which was in
 530 a region to the south of Greenland and Iceland.
 531 Further research will be carried out to determine
 532 the origin of the microseism and correlate those to
 533 microbaroms. Better statistics will be obtained by
 534 evaluating more than 1 year of data, by excluding,
 535 for example, special weather conditions.

536 In conclusion, the general behavior of an in-
 537 frasound array, like ARCI, can be understood
 538 by evaluating the detectability in relation to at-
 539 mospheric processes and source activity. Upper
 540 atmospheric winds and the state of the boundary
 541 layer play an important role in the detectability
 542 of infrasound. Understanding such dependencies
 543 is important for the identification of small-sized
 544 nuclear test which are expected to occur in the
 545 low-frequency or microbarom band.

546 **Acknowledgements** The work performed in this study
 547 was supported by a Transnational Access (TA) grant. This
 548 TA grant was provided by NERIES, an EC project with
 549 contract number RII3-CT-2006-026130. Figures in this ar-
 550 ticle were made with the Generic Mapping Tools (Wessel
 551 and Smith 1991).

552 References

553 Balachandran NM, Donn WL, Rind D (1977) Concorde
 554 sonic booms as an atmospheric probe. *Science* 197:47–
 555 49
 556 Dahlman O, Mykkeltveit S, Haak H (2009) Nuclear test
 557 ban. Springer, Dordrecht
 558 Drob DP, Picone JM, Garcés MA (2003) The global mor-
 559 phology of infrasound propagation. *J Geophys Res*
 560 108:4680
 561 Essen HH, Krüger F, Dahm T, Grevemeyer I (2003) On
 562 the generation of secondary microseisms observed in
 563 northern and central Europe. *J Geophys Res* 108:2506

Evers LG, Haak HW (2001) Listening to sounds from an
 564 exploding meteor and oceanic waves. *Geophys Res*
 565 *Lett* 28:41–44
 566
 567 Evers LG, Haak HW (2005) The detectability of infra-
 568 sound in the Netherlands from the Italian volcano Mt.
 569 Etna. *J Atmos Sol-Terr Phys* 67:259–268
 570
 571 Evers LG, Siegmund P (2009) Infrasonic signature of the
 572 2009 major sudden stratospheric warming. *Geophys*
 573 *Res Lett* 23:L23,808
 574
 575 Garcés MA, Willis M, Hetzer C, Le Pichon A, Drob D
 576 (2004) On using ocean swells for continuous infra-
 577 sonic measurements of winds and temperature in the
 578 lower, middle, and upper atmosphere. *Geophys Res*
 579 *Lett* 31:L19,304
 580
 581 Gossard EE, Hooke WH (1975) *Waves in the atmosphere*.
 582 Elsevier Scientific, Amsterdam
 583
 584 Hedlin MAH, Alcoverro B, D’Spain G (2003) Evaluation
 585 of rosette infrasonic noise-reducing spatial filters. *J*
 586 *Acoust Soc Am* 114:1807–1820
 587
 588 Holton JR (1979) *An introduction to dynamic meteorol-*
 589 *ogy*. Academic, London
 590
 591 Kedar SM, Longuet-Higgins MS, Webb F, Graham N,
 592 Clayton R, Jones C (2008) The origin of deep ocean
 593 microseisms in the North Atlantic Ocean. *Proc R Soc*
 594 *Lond A* 464:777–793
 595
 596 Le Pichon A, Ceranna L, Garés M, Drob D, Millet C (2006)
 597 On using infrasound from interacting ocean swells
 598 for global continuous measurements of winds and
 599 temperature in the stratosphere. *J Geophys Res* 111:
 600 D11,106
 601
 602 Le Pichon A, Vergoz J, Herry P, Ceranna (2008) Analyzing
 603 the detection capability of infrasound arrays in central
 604 Europe. *J Geophys Res* 113:D12,115
 605
 606 Le Pichon A, Vergoz J, Blanc E, Guilbert J, Ceranna L,
 607 Evers LG, Brachet N (2009) Assessing the perfor-
 608 mance of the international monitoring system infra-
 609 sound network: geographical coverage and temporal
 610 variabilities. *J Geophys Res* 114:D8112
 611
 612 Liszka L (1978) Long-distance focusing of concorde sonic
 613 boom. *J Acoust Soc Am* 64:631–635
 614
 615 Melton BS, Bailey LF (1957) Multiple signal correlators.
 616 *Geophysics XXII*:565–588
 617
 618 Posey JW, Pierce AD (1971) Estimation of nuclear explo-
 619 sion energies from microbarograph records. *Nature*
 620 232:253
 621
 622 Posmentier ES (1967) A theory of microbaroms. *Geophys*
 623 *J R Astron Soc* 13:487–501
 624
 625 Roth M, Fyen J, Larsen PW (2008) Setup of an experimen-
 626 tal infrasound deployment within the ARCES array.
 627 Scientific Report 2-2008, NOR SAR
 628
 629 Smart E, Flinn EA (1971) Fast frequency–wavenumber
 630 analysis and Fisher signal detection in real-time infra-
 631 sonic array data processing. *Geophys J R Astron Soc*
 632 26:279–284
 633
 634 Sutherland LC, Bass HE (2004) Atmospheric absorption
 635 in the atmosphere up to 160 km. *J Acoust Soc Am*
 636 115:1012–1032
 637
 638 Symons GJ (ed) (1888) *The eruption of Krakatoa and sub-*
 639 *sequent phenomena*. Trübner & Co., London
 640
 641 Wessel P, Smith WHF (1991) Free software helps map and
 642 display data. *EOS Trans AGU* 72:441

625 Whipple FJW (1930) The great Siberian meteor and the
626 waves, seismic and aerial, which it produced. Q J R
627 Meteorol Soc 56:287–304

Whipple FJW (1939) The upper atmosphere, density and 628
temperature, direct measurements and sound evi- 629
dence. Q J R Meteorol Soc 65:319–323 630

UNCORRECTED PROOF

AUTHOR QUERY

AUTHOR PLEASE ANSWER QUERY

Q1. Figures 5–8 were rasterized. Please check if captured appropriately.

UNCORRECTED PROOF